Ceramics International 48 (2022) 36789–36801

Contents lists available at ScienceDirect

Ceramics International

journal homepage: www.elsevier.com/locate/ceramint

Microstructure and properties of *in situ* TiC/Ni functionally gradient coatings by powder-fed laser cladding

Liaoyuan Chen, Ying Chen, Xin Chen, Tianbiao Yu *, Zixuan Wang

School of Mechanical Engineering and Automation, Northeastern University, Shenyang, 110819, China

ARTICLE INFO

Keywords:
TiC/Ni functionally gradient coating
In situ process
Size and content
Microstructure
Microhardness
Wear resistance

ABSTRACT

Powder-fed laser cladding with layer-by-layer deposition characteristics offers the unique advantages in the fabrication of ceramic/metal functionally gradient coatings (FGC). However, the inability of the size to vary with the content of the ceramics usually results in limited wear resistance or non-uniform mechanical properties of ceramic/metal FGC fabricated by the *ex-situ* process. Therefore, in this study, *in situ* synthesis of titanium carbide/nickel (TiC/Ni) FGC was carried out on ductile cast iron by powder-fed laser cladding using Ni45, Ti, and Ni-coated graphite (C). Seven groups of gradient compositions from 0 to 50% Ti + Ni-coated C with a Ti to C atomic ratio of 1:1 were designed. The phase composition, microstructure, interfacial characteristics between the consecutive layers, microhardness, and wear rate from the bottom to the top of the *in situ* synthesized TiC/Ni FGC were systematically studied. The results indicated that the phase composition was subjected to the desired evolution with the increase in the deposition height. Besides, the relative length and area fractions of ceramic compounds also gradually increased, following the quadratic and linear functions, respectively. The microhardness increased from the bottom to the top following a quadratic function: $Y = 2.961E-6X^2 + 0.0217X + 530.30$ with an R-square of 97.97%, and the wear rate decreased following a linear function: $Y = 4.873E-9X + 5.077E-5$ with an R-square of 94.04%. The maximum microhardness of 1036.25 HV and minimum wear rate of $4.872E-6$ $mm^3 \cdot N^{-1} \cdot m^{-1}$ were obtained at the top of the *in situ* TiC/Ni FGC. Besides, the wear mechanism also varied with the relative length and area fraction of the *in situ* TiC. This study confirms the feasibility of the fabrication process of the ceramic/metal FGC involving the size varies with the content of ceramics by *in situ* process.

1. Introduction

The advent of ceramic/metal functionally gradient coating (FGC) with continuous gradient behavior in microstructure and properties can not only meet the performance requirements corresponding to different locations of the part, but also relieve defects associated with poor bonding strength and rapid variation in properties at the metal/ceramic interface, where the damage always gets initiated [1,2]. Therefore, ceramic/metal FGCs can be utilized in a wide range of options for achieving the desired grading properties in machinery, aviation, aerospace, navigation, automobile, biomedicine, and other fields, [3–5]. Recently, ceramic/metal FGCs have attracted considerable research interest because of the boom of powder-fed laser cladding technology over the past two decades [6,7], which exhibits unique advantages in terms of unique layer-by-layer deposition characteristics, flexible component design, advanced deposition strategy, rapid response to market demands, and so on [8,9].

As early as 1993, five years after the concept of FGCs was proposed, Jasim et al. [10] reported a laser-clad Al–SiC FGC on an IN625 substrate using raw mixtures of Al–10, 30, and 50 wt% SiC, respectively. When the content of SiC was 10 wt%, undesired needle-like Al_4C_3 particles were found in the matrix due to the dissolution of SiC. However, round-shaped SiC particles were more prone to be retained at high volume fractions of SiC. Zhang et al. [11] fabricated two thin-walled FGCs using Ti to Ti-40 vol%TiC without a discrete interface on the Ti–6Al–4V plate by the continuous-wave CO_2 laser source. The un-melted TiC particles were embedded in the TiC/Ti FGC, and the microhardness increased from 220 HV to 450 HV along the build-up direction. Furthermore, Mahamood et al. [12] fabricated a TiC/-Ti6Al4V FGC with the TiC content varying from 0 to 50 vol% by laser metal deposition. The incompletely melted TiC particles at high volume fractions resulted in a large variation, approximately four times of the

* Corresponding author. School of Mechanical Engineering and Automation, Northeastern University, Shenyang, 110819, China.
E-mail address: tianbiaoyudyx@gmail.com (T. Yu).

https://doi.org/10.1016/j.ceramint.2022.08.243
Received 13 June 2022; Received in revised form 16 August 2022; Accepted 22 August 2022
Available online 27 August 2022

maximum value compared with that of the substrate. A similar microstructure and microhardness evolution were also found in a study by Li et al. [13]. The size of the unmelted TiC particles has an insignificant variation with the incremental TiC content. That is, at the bottom of TiC/Ti6Al4V FGC, the embedded coarse TiC particles are not uniformly spaced. Besides, some cracks were observed to penetrate the unmelted TiC and the matrix, resulting in low toughness.

For the systematic exploration of the process feasibility of ceramic/nickel FGCs and subsequent analysis of their microstructure and properties, related studies have been carried out extensively. Wilson and Shin [14] presented a laser direct deposition process to fabricate TiC/Inconel 690 FGC with the volume fraction of TiC particles varying from 0% to 49%. The drastic variation in microstructure with increasing TiC content resulted in the sudden fluctuations in the microhardness and volume loss in different positions of the FGC. Besides, the decomposition behavior of TiC particles under laser treatment was not observed. Shi et al. [15] firstly optimized the laser cladding process of Ni/WC by Taguchi's method. Subsequently, they fabricated a free-crack and pores gradient composite coating. The coarse WC particles (more than 50 μm) improved the surrounding hardness and wear resistance. Moreover, apparent interfaces were also observed between the layers. Wang et al. [16] prepared a three gradient Ni60/coarse WC FGC on Q345R steel, the improved wear resistance of the Ni60 coating was obtained. Unfortunately, the coarse WC ceramic particles mainly accumulated at the bottom of the tracks because of the high density. The fabrication process of other ceramics/metal FGCs with different ceramics, such as Invar/TiC [17], WC/Stellite 6 [18], ZrO_2/Ti6Al4V [19], W/Al [20], and corresponding microstructure and mechanical properties also have been reported. The analysis of the above-mentioned studies indicates that the process employed by most researchers for laser additive manufacturing (AM) of ceramic/metal FGC coatings is *ex-situ*, i.e. ceramic particles with different gradient content are briefly mixed with metal powder, and then the FGC with a single gradient direction is developed layer by layer through laser AM.

Nonetheless, there are several inherent limitations caused by the initial size of the ceramic particles when using the *ex-situ synthesis* technology to fabricate ceramic/metal FGCs via powder-fed laser cladding, as shown in Fig. 1, one of the most important aspects of FGCs is that their microstructure and properties would be varied in a gradient with the position. Therefore, it can be speculated that the size of the ceramic particles should be positively correlated with the content. When the ceramic content is low, the ceramic particles are expected to be fine due to the uniformity of the mechanical properties. In contrast, when the ceramic content is high, the ceramics are expected to be coarse due to the superior wear resistance. Moreover, the sharp interfaces between the *ex-situ* synthesized ceramics and matrix, where failure is always initiated, are also observed due to the poor wetting performance [21,22].

In recent years, with the gradual advancement of *in situ* synthesis process in the fabrication of composite coatings, there have been signs of a solution to the above-mentioned challenges. Wang et al. [23] fabricated a series of submicron Ti(C, N) particles reinforced coatings by synchronized powder feeding plasma transferred arc cladding technology with different mole ratios of Ti/g-C_3N_4 in the initial materials. The wear resistance and hardness tended to increase in a gradient manner with the molar ratio. Besides, the clear interface between the *in situ* formed Ti(C, N) and Fe_2Ti was also observed. TiC, Ti_5Si_3, and Ti_3SiC_2 with different sizes and content were *in situ* generated in the Ti6Al4V/(TiC + Ti_3SiC_2) FGC by Li et al. [24]. The diameter of *in situ* synthesized TiC particles increased firstly and then decreased with enhancement in the volume fraction of (Ti–Si–C). The microhardness also increased in a gradient manner. Jing et al. [25] fabricated TiC and TiB*x* referenced TiNi/Ti_2Ni-based gradient composites with the preset layer including different mixtures (TiNi + 10, 20, and 30 wt% B_4C). However, the wear resistance was affected by the presence of pores due

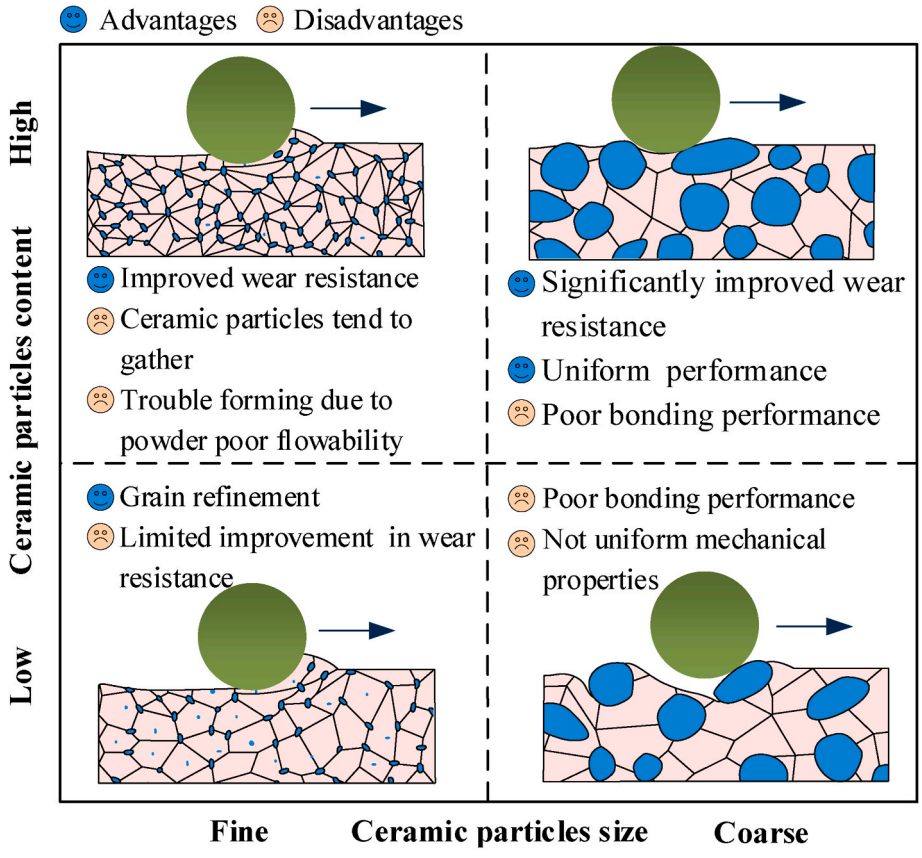

Fig. 1. Advantages and disadvantages of ceramic/metal FGCs synthesized by *ex-situ* process depending on the size and content of ceramic compounds.

to the oxidation of B_4C, and Zhao et al. [26] also observed a similar phenomenon. Moreover, several studies [27–29] have also confirmed the potential for the fabrication of *in situ* ceramic/metal FGCs by laser AM process. Interestingly, defects associated with poor bond strength and sharp variation in properties at the metal/ceramic interface are alleviated [30,31].

Titanium carbide (TiC) has proven to be a good candidate for fabricating ceramic/metal FGCs due to its high hardness [32] and excellent wear resistance [33] as well as good wetting behavior toward alloys [34]. However, the powder-fed laser cladding process, microstructure, and properties of TiC/Ni FGCs synthesized by *in situ* process have rarely been reported to date. In this study, Ti + Ni-coated graphite particles with gradient content variation were uniformly mixed in Ni45 powder. Subsequently, *in situ* synthesized TiC/Ni FGC with the parabolic trend in hardness and linear trend in wear rate was fabricated layer by layer via powder-fed laser cladding. Besides, the effect of *in situ* synthesized TiC particles with different sizes on the layer-to-layer microstructural evolution of TiC/Ni FGC was analyzed and discussed in detail.

2. Materials and methods

2.1. Material and setup

Spherical Ni45 powder particles with the diameter ranging from 13.41 μm to 130.61 μm (mean diameter of 64.66 μm), pure Ti particles with sizes ranging from 7.21 μm to 105.68 μm (purity 99.95%, mean length of 50.00 μm), and Ni-coated graphite (C) particles with sizes ranging from 26.87 μm to 139.88 μm (purity 99.95%, mean length of 68.76 μm) were selected as materials for deposition, where the mass ratio of C to Ni elements in Ni-coated C particles is 3:1. The elemental composition of spherical Ni45 powder particles is 0.45 wt% C, 12.00 wt % Cr, 4.00 wt% Si, 10.00 wt% Fe, 2.40 wt% B, 0.10 wt% Mn and balance Ni. The scanning electron microscopy (SEM) morphological characteristics and size statistics of the Ni45 powder, Ti, and Ni-coated C particles are shown in Fig. 2. The sizes of all powders are within the acceptable range of the powder feeder, so that the better flowability provides stability in the deposition process, resulting in fewer defects.

The experiments were carried out through a coaxial laser AM system, including a 500 W fiber laser generator with the wavelength of 1020 nm (IPG 500, Germany), a coaxial cladding nozzle (RC52), a disc powder feeder (PGF-1), a KUKA robot (KR16-2), and cooling equipment (Tongfei cooling, SL400), as shown in Fig. 2. The scanning strategies could be executed with high reliability due to the repeatability of the KUKA robot (±0.08 mm). The focus of the optical system and powder beam was located on a plane at a distance of 15.0 mm low the cladding nozzle, where the diameter of the laser beam was 1.0 mm. The mass of the output powder particles could be adjusted using the powder feeder with high sensitivity, suitable for particle sizes in the range of 44 μm to 149 μm (−100/+325 mesh).

2.2. Process and characterization

To validate the feasibility process and analyze the microstructure, microhardness, and wear rate of the *in situ* TiC/Ni FGC via laser AM, a series of progressive transformation steps were carried out, as shown below:

(1) Design powder component

The seven gradient compositions of *in situ* TiC were designed layer-by-layer with increasing ceramic content from the bottom to the top of the FGC, as shown in Fig. 2. The composition of raw powder for *in situ* synthesized TiC/Ni FGC is listed in Table 1, where the Ti/C atomic ratio is approaching 1:1. The composite powder was weighed, matched, and

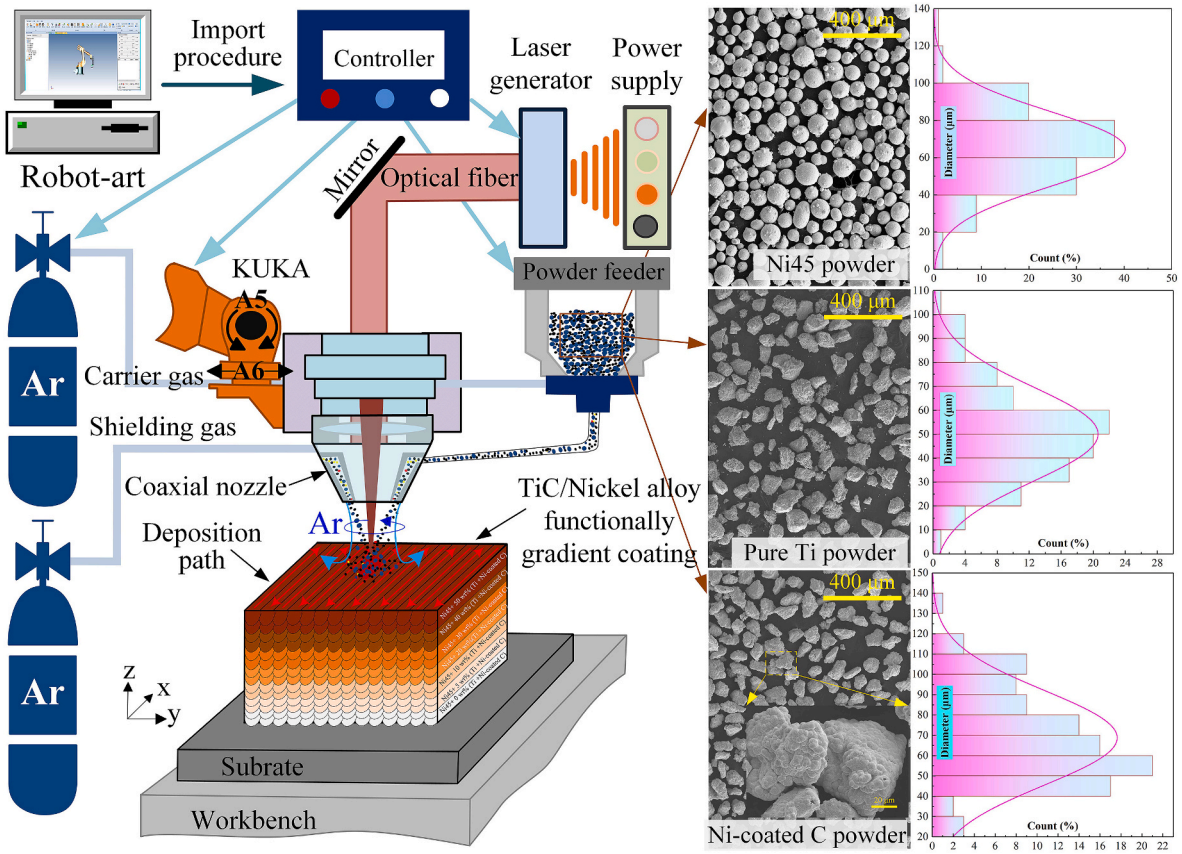

Fig. 2. The fabrication process of *in situ* TiC/Ni functionally gradient coating by powder-fed laser cladding.

Table 1
The component design of raw powder for *in situ* TiC/Ni FGC.

Layers	Corresponding zone	Powder composition design
1–2	I	100.0 wt%Ni45 + 0.00 wt% Ti + 0.00 wt% Ni-coated C
3–4	II	95.00 wt%Ni45 + 3.75 wt% Ti + 1.25 wt% Ni-coated C
5–6	III	90.00 wt%Ni45 + 7.49 wt% Ti + 2.51 wt% Ni-coated C
7–8	IV	80.00 wt%Ni45 + 14.98 wt% Ti + 5.02 wt% Ni-coated C
9–10	V	70.00 wt%Ni45 + 22.47 wt% Ti + 7.53 wt% Ni-coated C
11–12	VI	60.00 wt%Ni45 + 22.96 wt% Ti + 10.04 wt% Ni-coated C
13–14	VII	50.00 wt%Ni45 + 37.45 wt% Ti + 12.55 wt% Ni-coated C

then mixed in a planetary ball mill at a speed of 120 rpm for 100 min to avoid spherification.

(2) Design deposition strategies and program

The deposition path was designed in a 'BOW' to reduce the heat accumulation at the edges of the part because of single-direction deposition [35], as shown in Fig. 2. A three-dimensional (3D) model with the $20 \times 10 \times 10$ mm^3 was designed, sliced equally in layers, post-processed by using CAD software, and finally imported into the offline programming software (Robot-Art). The edges of the slices were identified, extracted, optimized, and simulated to generate the deposition path, which could be read by the control system of the KUKA robot.

(3) Carry out Experiments

Before the experiments, the mixed composite powders were preheated at 100 °C for 100 min to remove residual water vapor. The *in situ* TiC/Ni FGC was fabricated on the ductile cast iron with the $50 \times 50 \times 10$ mm^3. According to the literature study [36], the laser power, scanning speed, and powder feed rate were set as 425 W, 4.5 mm s^{-1}, and 0.85 r min^{-1}, respectively. After the deposition of each layer, the time interval was set as 2 min to reduce heat accumulation.

(4) Obtain microstructure and mechanical properties

The samples were cut from the substrate in a direction perpendicular to the scanning direction by EDM cutting equipment, as shown in Fig. 3. The metallographic sample was ground with four fine SiC grits (800, 1000, 1500, and 2000 mesh), and then polished using the polishing solution with a diamond particle size of 1.5 μm by a five-axis CNC polishing machine, until the surfaces were free of scratches. The polished plane was eroded in the etching solution containing 20 mL HNO_3 and 60 mL HCl for 20–40 s to distinguish the phase characterization. Before the tests, the sample was ultrasonically cleaned in alcohol for 120 s.

The graded microstructure was obtained by 3D microscopy (LEXT OLS4100, Japan). The field SEM (Zeiss, Germany) system equipped with a backscattered electron (BSE) detector and an energy dispersive spectroscopy (EDS) system was employed to obtain the microstructural and elemental characteristics. Besides, compounds were also detected by X-ray diffraction (XRD, PANalytical, Netherlands) with Cu Kα-radiation and 2θ ranging from 25° to 85° on the three polished *x-y* planes, where the distances from the interface were 2250 μm, 5250 μm, and 8250 μm, respectively.

The microhardness of the *in situ* TiC/Ni FGC was measured on the polished cross-section using a Vickers microhardness tester (HV-1000, China) with automatic focus. The load of 300gf and a dwell time of 10 s

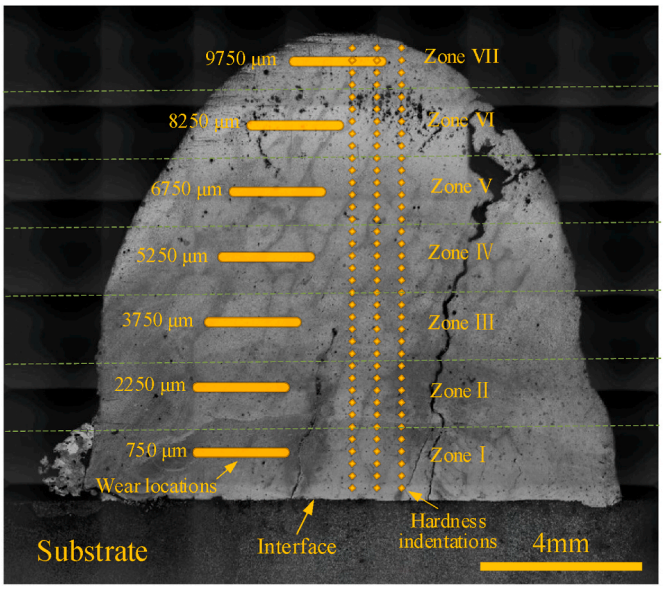

Fig. 3. Optical cross-section showing the test locations.

and an interval of 300 μm at the center regions were set separately. Data were collected automatically along the building direction, which resulted in the enhancement of work efficiency and reliability. The position of the indentations is shown in Fig. 3. To evaluate the reciprocating wear behavior of the *in situ* TiC/Ni FGC as a whole, the multifunctional material surface properties tester (MFT-4000, China) was employed. Seven sets of dry sliding wear tests were carried out on the cross-section at different positions, where the distance from the interface (*D*) is shown in Fig. 3. An Al_2O_3 ball of φ5 mm with a hardness of more than 90 HRC was selected as the counterpart material. Other parameters included a load of 10 N, sliding distance of 3 mm, speed of 200 r min^{-1}, and test time of 30 min. The 2D, 3D worn surfaces and volume loss (V_{loss}) at different positions of *in situ* synthesized TiC/Ni FGC were also obtained by the OLS4100 with powerful data processing capabilities. Besides, the wear rate, ω (mm^3/N/m) was obtained by using the formula $\omega = V_{loss}/FL$, where *F* and *L* represent the load force and total sliding distance, respectively.

(5) Analyze the microstructure and properties of the fabricated FGC to check process feasibility.

3. Results and discussion

3.1. Microstructure and elemental compositions

Fig. 4 demonstrates that the morphology of the microstructure in the TiC/Ni FGC evolved significantly with the increase in deposition height according to optical images and corresponding local magnification of BSE images. The optical image of the substrate exhibits a clear interface, which indicates that the TiC/Ni FGC was metallurgically well bonded to the substrate. The black particles in the substrate could be assigned to spherical graphite according to the EDS result of micro-zone I marked in Fig. 4a, as listed in Table 2. At the same time, some free spherical graphite particles were also observed at the foot of the TiC/Ni FGC, mainly attributed to the strong effect of Marangoni convection. Fig. 4b illustrates that Zone I follows the typical characteristics of a laser AM Ni45 coating and contains mainly γ-Ni, [Fe–Ni] solid solution, CrB, and Cr_7C_3 according to our previous study [36].

When 5% and 10% Ti + Ni-coated C particles were added to the raw materials, the size and number of the matrix (γ-Ni and [Fe–Ni] solid solution) at the bottom of TiC/Ni FGC decreased significantly, as shown in Fig. 4c and d. Besides, the microstructure exhibited two new types of

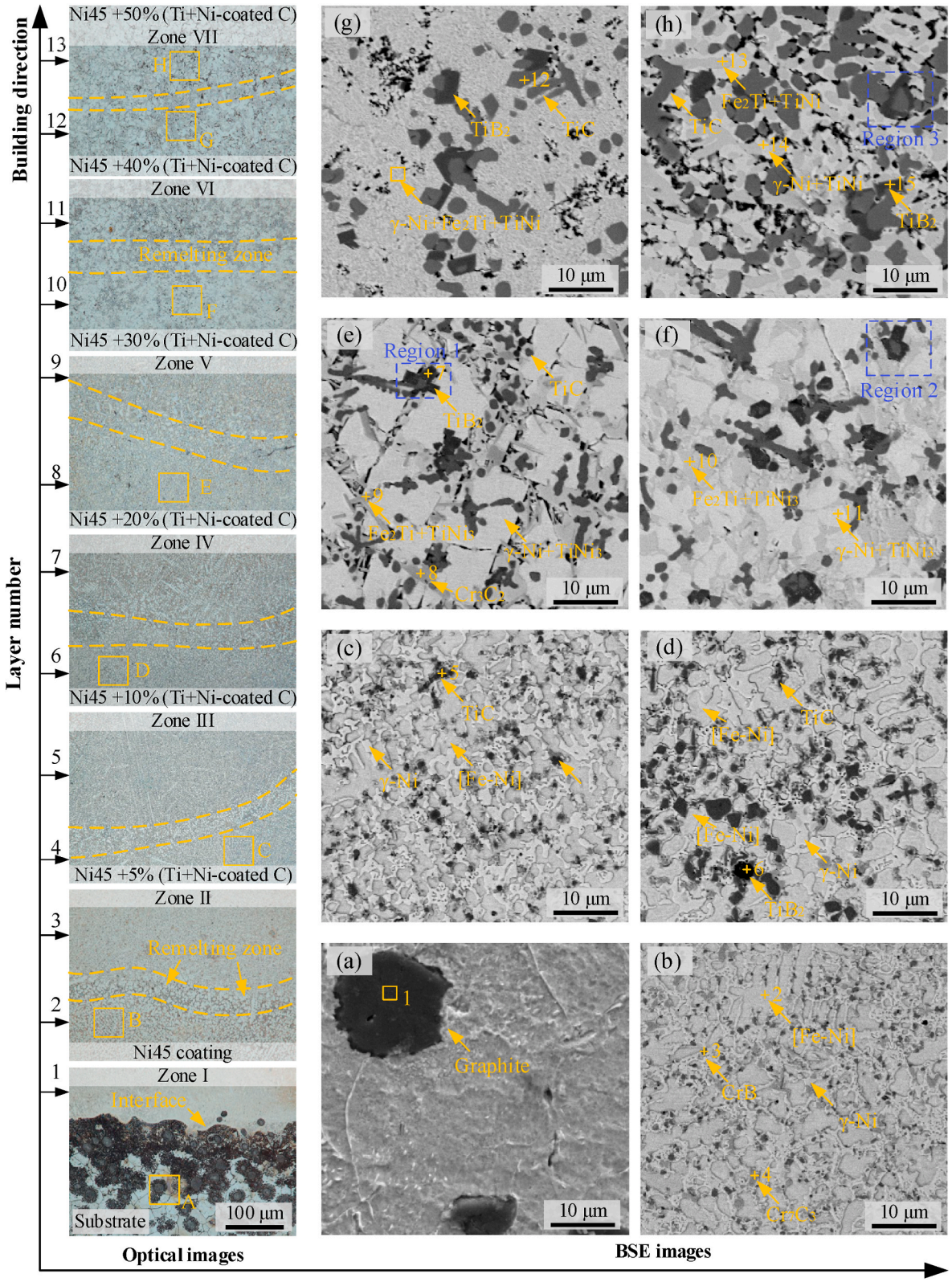

Fig. 4. The optical images and corresponding BSE images: (a) substrate, (b–h) zones I-VII.

fine black particles with spherical and polygonal shapes embedded at the boundaries of the grains. To identify these black phases, XRD and EDS were carried out. Fig. 5 indicates that Zone III is mainly composed of TiC, TiB_2, γ-Ni, and Cr_7C_3. The atomic ratio of Ti and C elements in Micro-zone 5 is 1:1. Moreover, Micro-zone 6 is rich in Ti and B elements with an atomic ratio of approximately 1:2. Thus, black spherical and polygonal phases could be identified as *in situ* synthesized TiC and TiB_2, respectively. The probability of binding between two elements as one compound was evaluated in terms of the Gibbs free energy (ΔG) [37] and the surrounding element concentration [38]. The ΔG of TiC and TiB_2 was negative over the temperature range from 0 °C to the corresponding melting point (3140 °C for TiC and 2980 °C for TiB_2) [39].

Table 2
EDS results marked in Fig. 4 (at. %).

Microzone	Ti	C	B	Cr	Si	Fe	Ni
1	–	100	–	–	–	–	–
2	–	–	–	8.6	3.9	26.71	60.79
3	–	–	30.51	30.41	2.52	15.2	21.36
4	–	21.93	–	49.21	0.48	15.17	13.21
5	45.78	48.22	–	2.97	0.43	1.58	1.02
6	23.89	4.15	63.48	2.55	0.68	0.72	4.53
7	39.56	45.26	13.94	0.82	–	–	0.42
8	3.56	21.68	6.2	30.29	0.89	6.64	30.29
9	26.37	11.42	4.50	8.56	7.68	6.02	35.45
10	25.35	11.56	8.75	8.34	6.97	5.83	33.20
11	25.46	24.48	3.98	3.19	1.71	2.14	39.04
12	48.28	45.26	–	2.01	0.53	0.46	3.46
13	25.35	11.56	8.75	8.34	6.97	5.83	33.20
14	25.37	25.53	2.91	3.08	1.71	2.11	39.29
15	28.46	12.89	46.59	4.23	0.35	3.46	4.02

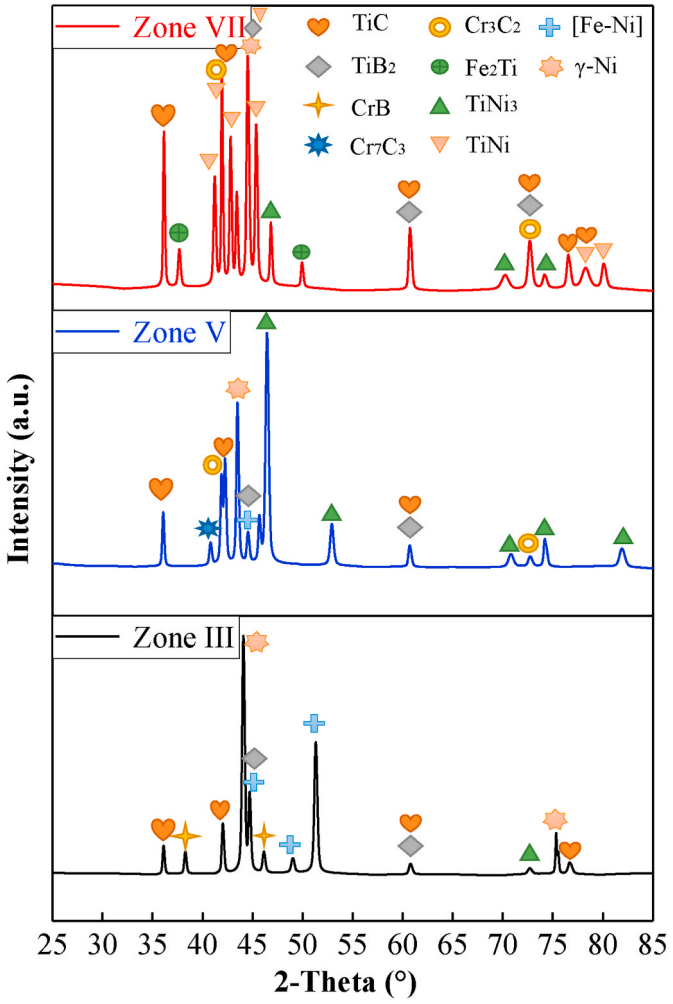

Fig. 5. XRD results of Zones III, V, and VII in Fig. 3.

Consequently, during the solidification process, the Ti element at the solidification front was allowed to combine spontaneously with the C and B elements to generate the crystal nucleation of TiC and TiB_2. The crystal nucleation of TiC with the face-centered cubic structures and TiB_2 with the hexagonal crystal structure grew up along their preferred orientations of $(111)_{TiC}$ and $(0001)_{TiB2}$ [40,41], resulting in spherical and polygonal morphologies, respectively. The previous study [40] had revealed that the fracture toughness of TiC–TiB_2 complexes is superior to that of single TiC ceramics. Therefore, the existence of the B element in the raw powder is beneficial in reducing the micro-cracks within the FGM coating.

Fig. 4e and f exhibit that the phase compositions in the middle of TiC/Ni FGC were almost identical when 20% and 30% Ti + Ni-coated C particles were added to the raw materials. Comparative analysis of the microstructural morphology at the bottom of the *in situ* synthesized TiC/Ni FGC, indicates the existence of some new phase. Zone V is composed of TiC, TiB_2, Cr_3C_2, Cr_7C_3, and $TiNi_3$ phases according to the XRD result, as shown in Fig. 5. The lump-shaped phases with gray color corresponded to Cr_3C_2 phases according to the EDS result of Micro-zone 8 and EDS results of Zone V. Although the ΔG of Cr_7C_3 was significantly less than that of Cr_3C_2 [42], the Cr element combined mainly with the progressively higher content of C element to form Cr_3C_2 rather than Cr_7C_3 as C element gradually dominated the competition during the solidification process. Besides, new needle-like phases and blocky phases (matrix) with white color were identified as $Fe_2Ti + TiNi_3$ and γ-Ni + $TiNi_3$, respectively, due to the progressively higher concentration of Ti element in the molten pool. Moreover, the TiC and TiB_2 particles became coarser due to the increasing concentration of Ti and C elements.

Fig. 4g and h show that the TiC and TiB_2 particles are the largest, with lengths of more than 2 μm. Besides, the TiC, TiB_2, Cr_3C_2, Fe_2Ti, and TiNi phases are *in situ* generated at the top of *in situ* formed TiC/Ni FGC, as shown in Fig. 5. To further analyze each phase and the corresponding elemental distribution, the EDS map scanning analyses were carried out. As shown in Fig. 6, the distribution characteristics of Ti, C, and B elements provide further evidence that the black spherical and polygonal particles are TiC and TiB_2 phases, respectively. Besides, the cellular dark gray phase shown in Fig. 6a primarily contains Fe, Ti, and Ni elements. Integration of the EDS result of Micro-zone 13 (listed in Table 2), XRD results of Zone VII, and the crystal characteristics of TiNi and Fe_2Ti [25,37]. It can be confirmed that the phases are Fe_2Ti + TiNi phases. Interestingly, almost all the TiB_2 phases are surrounded by TiC phases, in particular, in regions 1, 2, and 3 (Fig. 4) where this phenomenon should be more emphasized. The previous researchers [25,39] had found that the ΔG of TiB_2 is lower than that of TiC by roughly 100 kJ mol^{-1}, indicating that TiB_2 presents the most significant formation trend. Besides, the lattice mismatch factor of 1.001% between TiC and TiB_2 was much smaller than the criterion of 6.0% [37,43]. It indicates that TiC could use preferentially precipitated TiB_2 as its effective nucleation site and its growth was dependent. Based on the ΔG of various reactions to generate TiC and TiB_2 reported in the literature [43,44], it can be inferred that the C atom in TiC can be taken by the free B atom to form TiB_2 and similarly, the B atom in TiB_2 can be replaced by the free C to form TiC. Therefore, TiC and TiB_2 phases are grown independently, resulting in the TiC/TiB_2 composites.

Based on the above-mentioned analysis, the microstructure evolution from the bottom to the top of *in situ* TiC/Ni FGC is as follows: [Fe–Ni] solid solution, CrB, Cr_7C_3 → γ–Ni, $TiNi_3$, Cr_7C_3, Cr_3C_2, TiC, TiB_2 → TiNi, Cr_3C_2, Fe_2Ti, TiC, TiB_2. Moreover, the size of the reinforcements increases gradually, eventually to more than 2.0 μm at the top of the *in situ* formed TiC/Ni FGC.

The interfacial characteristics of FGCs not only govern the smooth transition of the mechanical properties but also act as a major factor in fatigue life [45]. Fig. 4 exhibits that the *in situ* TiC/Ni FGC shows good bonding properties with the substrate, without any microscopic cracks or pores. Besides, the size and content of the *in situ* TiC increase with the deposition height. However, the sharp transition in the microstructure of the remelting zone between the consecutive layers is significantly reduced. At the top of the *in situ* TiC/Ni FGC, the microstructure of the remelting zone is almost identical to that in the deposited layer. Compared to the conclusions from the previous studies [16,18,21], the sharp interface, where fatigue damage always occurs, is markedly inhibited. Therefore, to reveal the effect of *in situ* formed TiC on the interfacial characteristics of TiC/Ni FGC, a schematic illustration was obtained, as shown in Fig. 7. Based on the temperature distribution characteristics [30,38], the molten pool could be roughly divided into

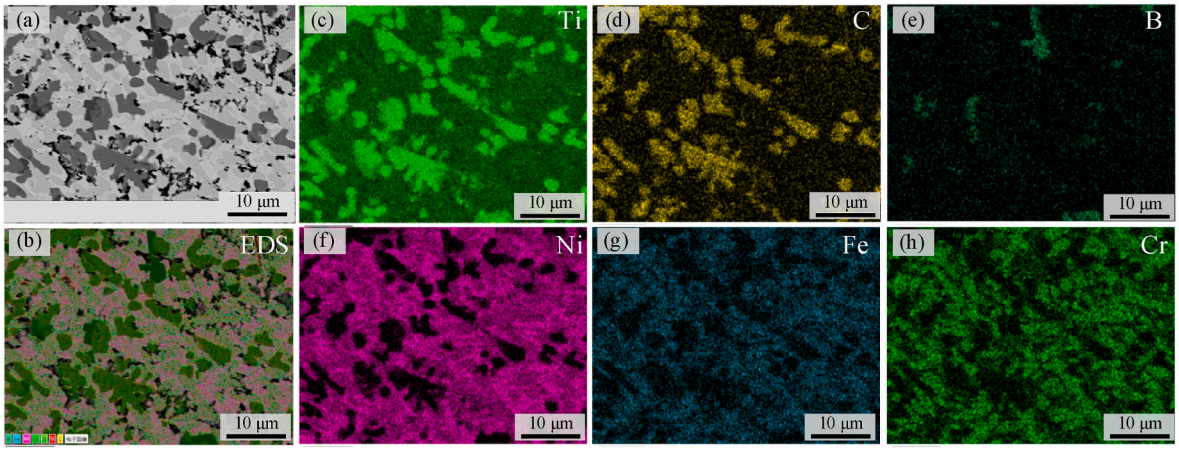

Fig. 6. (a) SEM image, (b) EDS image, and (c–f) element distribution of zone VII in Fig. 4.

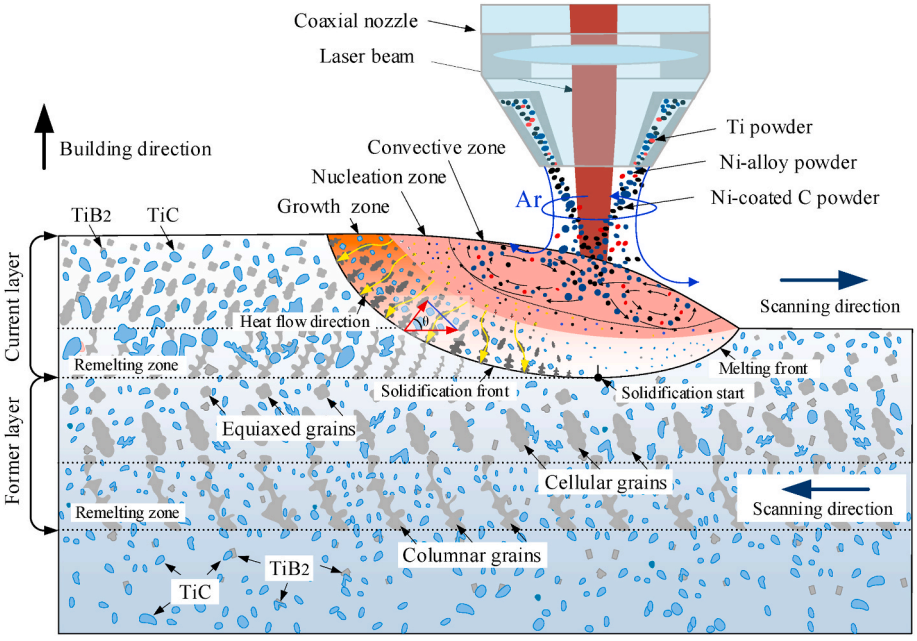

Fig. 7. Schematic illustration of the effect of *in situ* TiC on the microstructure of the remelting zone between the layers of TiC/Ni FGC.

the following three zones: convection zone, nucleation zone, and growth zone. The convection zone has the highest temperature, and in this zone, the injected materials are completely melted and uniformly transported to the molten pool. With the decrease of temperature, the nucleation zone begins to evolve, where the reinforcements such as TiC and TiB_2 are generated sequentially. Finally, the nucleation of reinforcements combined with the surrounding elements gradually grows in the growth zone. By the time the temperature is gradually reduced to room temperature, the microstructure evolution gets completed. The grain morphology prepared by laser AM is governed by two widely accepted factors on the solidification front: temperature gradient (G) and solidification rate (R) [46–48]. The value of G relies on heat dissipation of the molten state, while the R can be expressed as $R = V{\cdot}\cos\theta$ [49], where θ is illustrated in Fig. 7. In laser fabricated parts with a gradient transition from one alloy to another, orientated coarse columnar crystals are often found at the bottom of a single deposition layer with large G value due to good heat dissipation and small R owing to the small curvature of the solidification front [50,51]. The thermal conductivity of ceramics is significantly lower than that of metallic materials. On the one hand, the heat dissipation in the direction of the G gets inhibited by the uniformly distributed ceramic particles, resulting in lower G value. Therefore, the generation of columnar crystals is severely restricted. On the other hand, the preferential precipitation of the ceramic particles not only increases the nucleation sites of the crystals but also leads to pinning effects to crowd out the growth space of the columnar crystals. Therefore, the desired transition from columnar to equiaxed crystals was carried out in the remelting zone, thus the microstructure in the single deposition layer did not exhibit any particular crystallographic orientation. This phenomenon becomes increasingly more pronounced with the increase in the size and content of the ceramic particles with the deposition layer. Consequently, the bonding interface between the consecutive layers becomes smoother.

3.2. Ceramic contents and size analysis

The content and geometric characteristics of the ceramic particles are the main contributing factors to the mechanical properties of the *in situ* TiC/Ni FGC. Therefore, Image-Pro Plus 6.0 was employed to identify the characteristics of ceramic particles and to count their area fraction and relative length, and the results are shown in Fig. 8. With a gradual

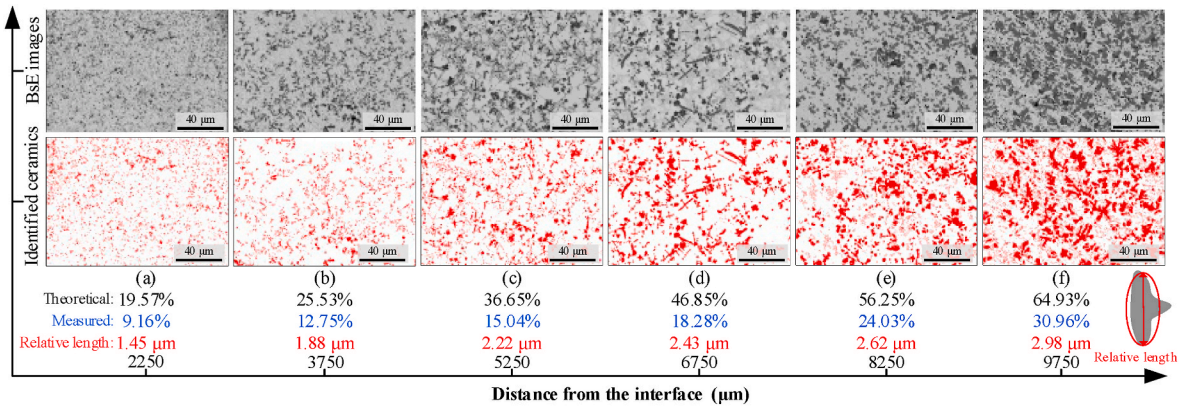

Fig. 8. Identified ceramic particles and corresponding area fractions and relative length at the different zones.

increase in Ti and Ni-clad graphite content, the area fraction of ceramic particles gradually increased from 9.16% at the bottom of the FGC to 30.96% at the top of the FGC, following a quadratic function: $Y = 3.137E-7{\cdot}X^2 - 7.728E-5{\cdot}X + 9.957$ with an R-square of 98.80%. It is generally believed that in-situ synthesized TiC particles would float to the surface of the single track under the effect of strong Marangoni convection due to low density [26]. However, the ceramic content of the *in situ* synthesized TiC/Ni FGC coating fabricated in this study varies very smoothly with the deposition height, as shown in Fig. 8. On the one hand, the Ti element with high chemical activity could easily react with oxygen to form oxides in the molten pool [52]. Some of these oxides, which do not have enough time to escape, adhere to the surface of the FGC, leading to low surface smoothness [39]. Combining the results of Zhou et al. [53] and the enriched Ti element in the molten pool, the oxide layer could be riched in TiO_2. As shown in Fig. 7, during the subsequent laser cladding process, these oxide particles on top surfaces are drawn into the molten pool and decomposed to increase the concentration of the Ti element due to its low melting point of 1840 °C. Therefore, the ceramic content at the bottom of the single track is increased. On the other hand, since the exposed area between the molten pool and the air becomes larger as it is closer to the surface of the molten pool, the oxidation of the Ti particles becomes more serious, resulting in a slight decrease in the ceramic content. Based on the above analysis, the oxidation of Ti elements is beneficial to increasing the gradient transition of ceramic content. It is noted that the measured volume fraction of ceramic particles is only about half of the theoretical value. Most of the oxides, which are riched in Ti element, are blown out of the molten pool under the action of strong shielding gas due to their low density. Therefore, the oxidation of Ti decreases the concentration of element Ti in the molten pool, resulting in the volume fraction of the obtained ceramic phases being much smaller than the theoretical value, as shown in Fig. 8. In addition, the rapid cooling rate usually results in insufficient *in situ* reaction between elements. This is another factor in which the fabrication of high-volume fraction of *in situ* synthesized ceramic phases is limited by laser AM technology. According to the literature [39,54], ceramic particles with a large aspect ratio in the composites exhibit better wear resistance. Therefore, the relative length of ceramic compounds was automatically measured according to the presentation in Fig. 8. It can be found that the relative length of ceramic compounds gradually increased from 1.45 μm at the bottom of the FGC to 2.98 μm at the top of the FGC, following a linear function: $Y = 1.914E-4{\cdot}X + 1.114$ with an R-square value of 98.18%. These findings confirm the process feasibility of fabricating ceramic/alloy FGC by *in situ* synthesis technology. Besides, the gradients in ceramic content and size also indirectly indicate that the reaction between Ti and C elements is sufficient due to their strong affinity for each other during the solidification process [44,55].

3.3. Microhardness

High hardness is a potentially important signature of the FGCs, indicating excellent wear performance because the wear resistance of the materials is strongly related to their hardness [56,57]. The microhardness distribution from the bottom to the top surface of the *in situ* TiC/Ni FGC can be found in Fig. 9. In the meanwhile, the corresponding microstructure around indentations reveals the effect of content and size of the *in situ* TiC on the microhardness variation. The results indicate that the microhardness of the *in situ* TiC/Ni FGC increased gradually from 556.85 HV on the Ni45 alloy side to 1036.25 HV at the twelfth layer with the *in situ* TiC content of 30.96% and the corresponding relative length of 2.98 μm, which presents an increased value of 85.91%. Compared with previous studies [11,15,16] on FGCs synthesized by *ex-situ* process, the microhardness of FGC fabricated by *in situ* process exhibits a smoother transition between the consecutive layers. Besides, the microhardness value of *in situ* fabricated TiC/Ni FGC with the increasing value of *D* can be expressed as: $Y = 2.961E-6{\cdot}X^2 + 0.0217{\cdot}X + 530.30$ with an R-square of 97.97%. The phenomenon which no step in microhardness between consecutive layers indicates that the stress and strain acting on the surface of the FGC can be passed uniformly to the interior, which can inhibit fatigue damage on the subsurface [58,59].

The gradient increase in microhardness of *in situ* TiC/Ni FGC is dependent on the microstructural evolution and phase composition. When 5 wt% Ti and Ni-coated C particles were added to the Ni45 alloy, some fine spherical TiC particles with a relative length of 1.45 μm were *in situ* generated in Zone II. Besides, the addition of Ni-coated C led to an

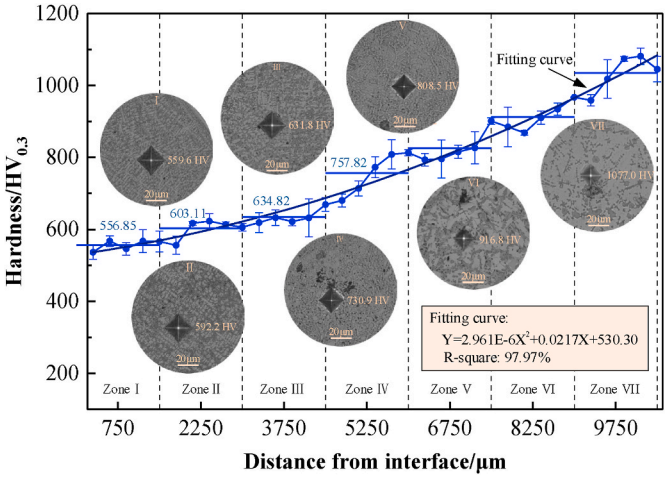

Fig. 9. The microhardness profile and corresponding indentations.

increase in the content of CrB and Cr_7C_3. On the one hand, the *in situ* formed TiC with a high hardness of 3200 kg/mm^2 plays the role of solid solution strengthening, resulting in the improvement of resistance to deformation. The grain size of the matrix of region II (Fig. 4c) is significantly smaller than that of region I (Fig. 4b). This also indicates that the resistance to external deformation in region II becomes stronger [39], and fine grain strengthening was achieved. Therefore, the mean microhardness of Zone II is more than 46.23 HV higher than that of Zone I. Fig. 8 illustrates that the size and area fraction of uniformly distributed reinforcements increased significantly with the gradual enhancement of added Ti and Ni-coated C particles. Besides, Marangoni convection could easily derive the uniform distribution of fine TiC particles, resulting in the dispersion strengthening effect on the soft matrix. Moreover, the cyclic evolution of the microstructure in the remelting zone was also suppressed by the *in situ* synthesis of the reinforcement, as shown in Fig. 7. Therefore, the variability of microstructure characteristics between consecutive layers is reduced and the microhardness distribution becomes smoother.

3.4. Wear resistance

To evaluate the wear resistance and reveal the corresponding wear mechanisms in different zones of the *in situ* fabricated TiC/Ni FGC, friction coefficients (COF), wear rates, and 2D and 3D worn surfaces were obtained. Fig. 10 illustrates the COF curves of the seven zones in TiC/Ni FGC. All curves pass through the "running in" period, where the COF is usually high, and then into the steady stage after about 10 min. The slight increment and fluctuation of the COF at the binging of the wear test can be attributed to the plastic deformation of the micro-bumps on the surface, the damage of the polished surface, and the small contact area between the friction pairs [60,61]. With the gradual removal of the surface material by shearing or flaking off, the soft matrix, carbides, and borides with high hardness were against the Al_2O_3 grinding ball and entered a steady stage, resulting in a stable COF. Noteworthy, the fluctuations in COFs in Zones V, VI, and VII are intense compared to those in the other Zones. This phenomenon can be attributed to the spalling of reinforcements or poor densification of composites [16,62]. The average friction coefficients obtained for each region during the steady stage are shown in Fig. 11. When the Ti and Ni-coated C particles were added at less than 20 wt%, the COFs in the corresponding zones decreased less than that of Ni45 alloy (0.619). However, when the Ti and Ni-coated C particles were added at more than 30 wt%, the COFs increased compared to that of the Ni45 alloy. This is assumed

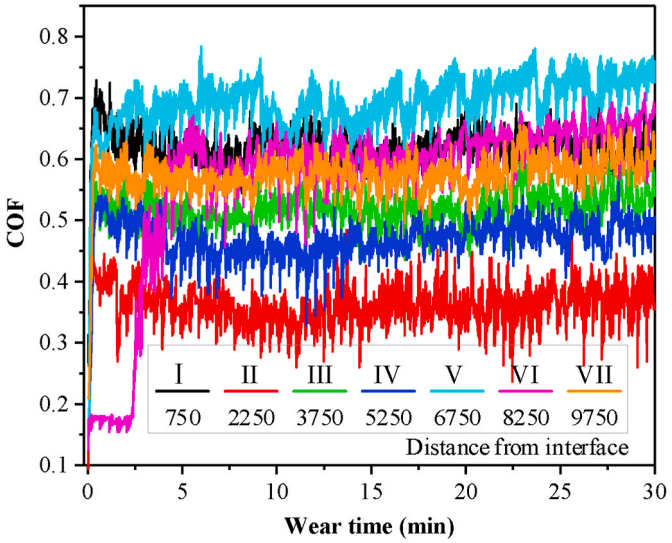

Fig. 10. The COF via wear time in different zones.

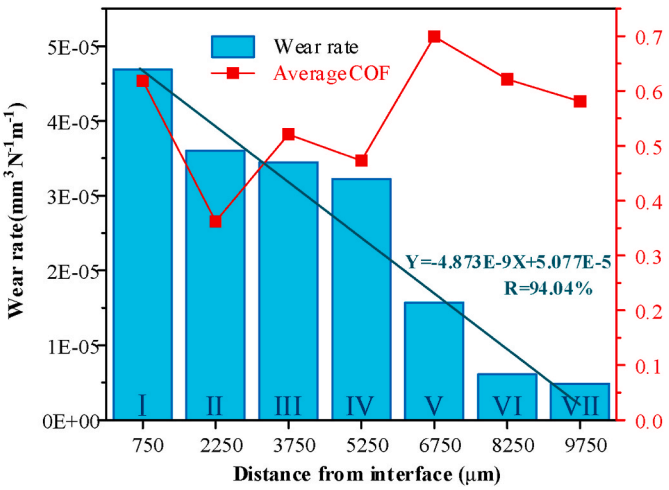

Fig. 11. Average COF and corresponding wear rate in different zones.

to be a transformation in the wear mechanism when the content and relative length of ceramic compounds are more than 18.28% and 2.43 μm, respectively.

Fig. 11 exhibits the wear rate in the different zones. The results indicate that the wear rate decreases in a gradient with increasing D, satisfying a linear regression equation: $Y = 4.873E - 9 \cdot X + 5.077E - 5$ with an R-square of 94.04%. The minimum wear rate of 4.872E-6 mm^3 N^{-1} m^{-1} is found at the top of the *in situ* TiC/Ni FGC, which is 10.39% of the wear rate of Ni45 alloy at the bottom of *in situ* formed TiC/Ni FGC. This has positive implications for the practical application of FGCs in terms of exhibiting excellent wear resistance. Besides, the COF and the wear rate do not correspond in a one-to-one manner, which is against Archard's law [63]. The contours of wear tracks at D = 750 μm, 3750 μm, and 8250 μm were obtained to reveal this interesting finding, and the results are shown in Fig. 12. The width, depth, and section area of the Ni45 wear track are 298.168 μm, 3.745 μm, and 1031.528 μm^2, respectively. Owing to low hardness, large plastic deformation is found on the worn surface in Zone I under the large contact stress of the Al_2O_3 grinding ball [36]. With the increase in the content of Ti and Ni-coated C particles, all these characteristics gradually decrease. *In situ* formed TiC, TiB_2 ceramic particles, some CrC_x, and intermetallic compounds (TiN and $TiNi_3$) demonstrate a progressive enhancement in solid solution, dispersion, and fine grain strengthening, decreasing wear rate. Noteworthy, although the worn surface of Zone III is rougher than that of the Ni45 alloy, material removal is the result of the interaction of plastic deformation and shearing. Therefore, the low deformation resistance of the material results in a gradual reduction in the COF. Fig. 12c shows that the *in situ* formed coarse ceramic particles prevent plastic deformation and can combine with the surrounding matrix to form some bumps on the worn surface. These bumps can prevent the relative sliding of the grinding ball and therefore increase the friction, resulting in a higher COF.

For correlation between the wear mechanism and the wear rate, the larger magnification 2D worn surfaces of *in situ* fabricated TiC/Ni FGC were obtained, as shown in Fig. 13. The worn surface of Ni45 alloy is uniformly distributed with continuous plow-like grooves along the sliding direction, and the distance between the peak and the valley on the section profile is 1.205 μm, demonstrating typical characteristics of adhesive wear.Fig. 13a1 represents that the worn surface of Ni45 alloy is quite smooth, which indicates that the bottom of the low hardness FGC is subjected to significant plastic deformation under high contact stresses. Besides, some flaky debris is also detected on the worn surface. Laser AM has the characteristic of rapid heating and cooling and therefore results in large local residual stresses within the part [64,65]. Under the repetitive attack of the grinding ball, the local residual stress

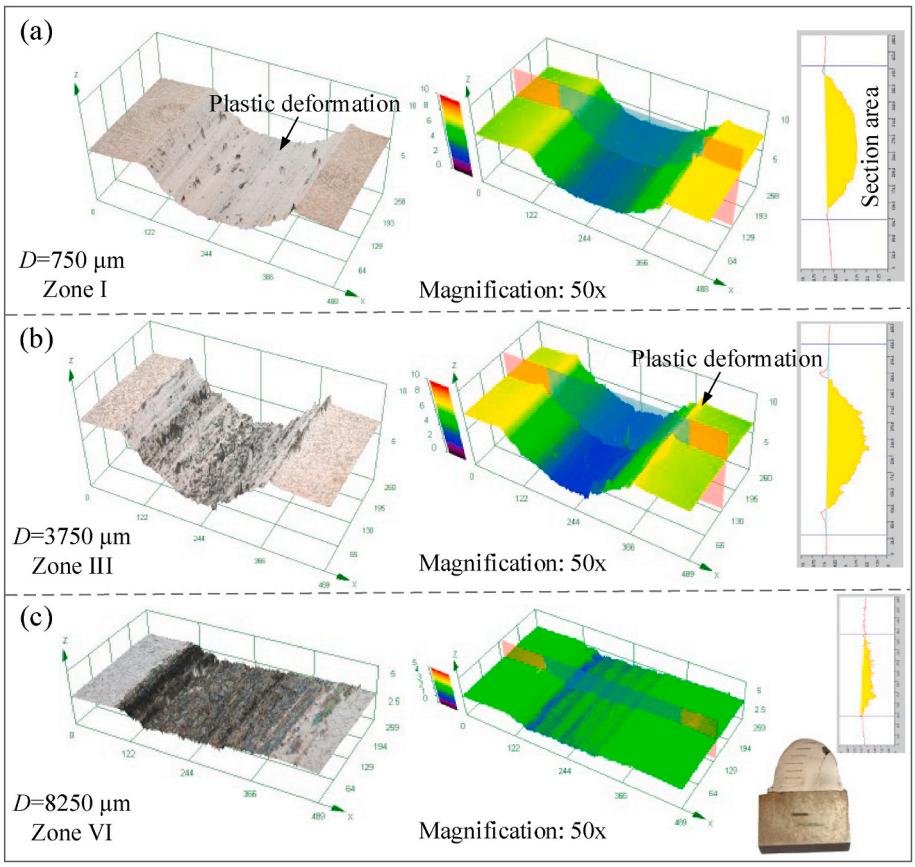

Fig. 12. 3D worn surface and corresponding section profile in Zones I, III, and VI.

encourages the development and expansion of the cracks at the subsurface of the worn surface. As wear progresses, the highly adhesive nickel alloy eventually develops flaky debris under shear stress. Fig. 13b shows that the characteristics of the worn surface in Zone III are significantly altered when the Ti and Ni-coated C particles were added at 20 wt%. Some flaky pits by local material spalling and long strip broken grooves by abrasive scratching alternate on the worn surface, which indicates that the *in situ* ceramic compound changes the wear mechanism. This is the combined effect of adhesive and abrasive wear. Notably, only a few coarse TiC particles, as the main reinforcements, are distributed on the worn surface in Zone III. More fine TiC particles are eventually removed by being embedded in the chips as their relative length of 1.88 μm is so fine to be smaller than the micro-cutting interface [66]. These chips, which contain hard particles with a hard center and soft edges, are eventually formed into near-spherical abrasive grains by the repeated pressing of the grinding ball. The abrasive grains were scratched against the surface of Zone III, which resulted in the formation of broken grooves with a maximum depth of over 1.5 μm, as shown in Fig. 13b2. Therefore, although the *in situ* formed ceramic particles with high hardness and good wear resistance form a good metallurgical bond with the matrix, the enhancement of wear resistance in Zone III is limited due to its small size, as shown in Figs. 11 and 12. Fig. 13c demonstrates that numerous smooth blocky areas are evenly distributed on the worn surface in Zone VI, where the relative diameter and content of TiC particles increase to 2.62 μm and 24.03%, respectively, while some shallow and narrow plow-like grooves are found in the gaps. Comparative analysis of morphological characteristics of TiC particles in Figs. 4 and 6, indicates that these blocky phases are *in situ* TiC. This result indicates that the *in situ* formed TiC particles with metallurgical bonding with the matrix were not removed as they were coarse enough to be larger than the micro-cutting interface. The coarse TiC particles with a relative length of over 2.62 μm acted as a skeleton, inhibiting the removal of the matrix. Besides, with the increase in the content of Ti and C, the matrix of the *in situ* fabricated TiC/Ni FGC FGC also transformed from γ-Ni to intermetallic compounds ($TiNi_3$ and TiNi), contributing to the wear resistance at the top of the FGC [25,41]. Therefore, the maximum profile height was also reduced from 2.216 μm in Zone III to 1.222 μm in Zone VI. The sufficiently large size of the TiC particles and the good bonding properties to the matrix ultimately result in only a small amount of material spalling on top of the *in situ* fabricated TiC/Ni FGC during the wear process, showing integrated characteristics of abrasive and fatigue wear.

4. Conclusions

This study investigated the process feasibility of the *in situ* fabricated TiC/Ni FGC based on the variation in size with the content of reinforcements by powder-fed layer-by-layer laser cladding using Ni45, Ti, and Ni-coated C powders. A detailed analysis of the effect of the geometrical characterization of the *in situ* ceramic compounds on interfacial characteristics, microhardness, and wear resistance was carried out. Based on the results of this study, the positive findings are listed as follows:

1. Phases evolved from the bottom to the top of the *in situ* TiC/Ni FGC as follows: [Fe–Ni] solid solution, CrB, Cr_7C_3 →γ–Ni, $TiNi_3$, Cr_7C_3, Cr_3C_2, TiC, TiB_2 → TiNi, Cr_3C_2, Fe_2Ti, TiC, TiB_2 with the increase of C/Cr and Ti/Ni ratio. Besides, the area fraction and relative length of the ceramic compounds increased in a gradient, following the quadratic and linear functions, respectively. Furthermore, their maximum values of 30.96% and 2.98 μm were obtained at the top of the *in situ* formed TiC/Ni FGC.
2. With the increase in the deposition height, particular crystallographic orientation was not observed and grain size was significantly

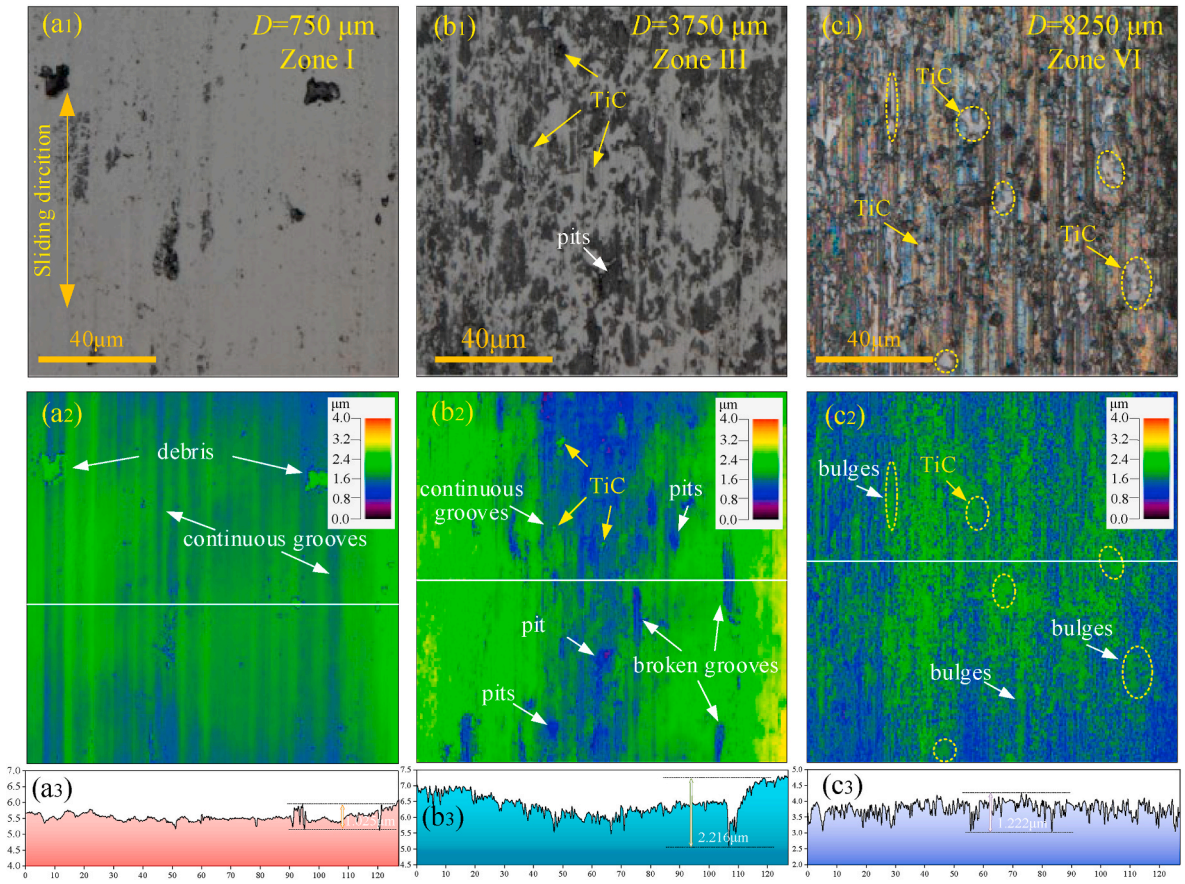

Fig. 13. 2D worn surface morphologies in Zones I, III, and VI.

reduced. In situ TiC particles with increasing size and content gradually weakened the heat flow density and decreased the temperature gradient at the bottom of the molten pool, resulting in the desired transition from columnar to equiaxed crystals. Therefore, the sharp transition in the microstructure between the consecutive layers was significantly decreased.

3. The microhardness of the TiC/Ni FGC increased gradually from the minimum value of 556.85 HV at the bottom of FGC to the maximum value of 1036.25 HV at the top of FGC, following a quadratic curve function: $Y = 2.961E-6 \cdot X^2 + 0.0217 \cdot X + 530.30$ with an R-square of 97.97%. The gradual increase in microhardness was the result of the enhancement of solid solution, fine grain, and dispersion strengthening of the coarser TiC particles.
4. Although the friction coefficient in the corresponding zones was slightly increased for Ti and Ni-coated C particles with the content of more than 30 wt%, the wear rate decreased continuously to a minimum value of $4.872E-6$ mm^3 N^{-1} m^{-1} with the increase in the deposition layer, following the quadratic function: $Y = 4.873E-9 \cdot X + 5.077E-5$ with an R-square of 94.04%. The relative length of *in situ* TiC particles was required to be larger than the micro-cutting interface (2.62 μm) to effectively decrease the wear rate. Besides, the wear mechanism was transformed from adhesive wear to abrasive wear and eventually to abrasive and fatigue wear.

Declaration of competing interest

The authors declare that they have no known competing financial interests or personal relationships that could have appeared to influence the work reported in this paper.

Acknowledgment

This work was supported by the Fundamental Research Funds for the Central Universities (N2103004); the National Natural Science Foundation of China (52075088).

References

[1] R. Fathi, H. Wei, B. Saleh, N. Radhika, J. Jiang, A. Ma, M.H. Ahmed, Q. Li, K. K. Ostrikov, Past and present of functionally graded coatings: advancements and future challenges, Appl. Mater. Today 26 (2022), 101373, https://doi.org/10.1016/j.apmt.2022.101373.
[2] Y. Hu, W. Cong, A review on laser deposition-additive manufacturing of ceramics and ceramic reinforced metal matrix composites, Ceram. Int. 44 (2018) 20599–20612, https://doi.org/10.1016/j.ceramint.2018.08.083.
[3] I.M. El-Galy, M.H. Ahmed, B.I. Bassiouny, Characterization of functionally graded Al-SiCp metal matrix composites manufactured by centrifugal casting, Alex. Eng. J. 56 (2017) 371–381, https://doi.org/10.1016/j.aej.2017.03.009.
[4] X. Chen, L. Gu, B. Zou, Y. Wang, X. Cao, New functionally graded thermal barrier coating system based on LaMgAl11O19/YSZ prepared by air plasma spraying, Surf. Coat. Technol. 206 (2012) 2265–2274, https://doi.org/10.1016/j.surfcoat.2011.09.076.
[5] W. Wu, J. Wang, Q. Liu, H. Xiao, X. Li, Y. Zhou, H. Wang, A. Zheng, J. Zhao, L. Ren, G. Li, Electrochemical polishing assisted selective laser melting of biomimetic superhydrophobic metallic parts, Appl. Surf. Sci. 596 (2022), 153601, https://doi.org/10.1016/j.apsusc.2022.153601.
[6] N. Shamsaei, A. Yadollahi, L. Bian, S.M. Thompson, An overview of Direct Laser Deposition for additive manufacturing; Part II: mechanical behavior, process parameter optimization and control, Addit. Manuf. 8 (2015) 12–35, https://doi.org/10.1016/j.addma.2015.07.002.
[7] L. Zhu, P. Xue, Q. Lan, G. Meng, Y. Ren, Z. Yang, P. Xu, Z. Liu, Recent research and development status of laser cladding: a review, Opt Laser. Technol. 138 (2021), 106915, https://doi.org/10.1016/j.optlastec.2021.106915.
[8] Z. Tong, X. Pan, W. Zhou, Y. Yang, Y.X. Ye, D. Qian, X. Ren, Achieving excellent wear and corrosion properties in laser additive manufactured CrMnFeCoNi high-entropy alloy by laser shock peening, Surf. Coating. Technol. 422 (2021), 127504, https://doi.org/10.1016/j.surfcoat.2021.127504.
[9] M. Ansari, E. Jabari, E. Toyserkani, Opportunities and challenges in additive manufacturing of functionally graded metallic materials via powder-fed laser

directed energy deposition: a review, J. Mater. Process. Technol. 294 (2021), 117117, https://doi.org/10.1016/j.jmatprotec.2021.117117.
[10] K.M. Jasim, R.D. Rawlings, D.R.F. West, Metal-ceramic functionally gradient material produced by laser processing, J. Mater. Sci. 28 (1993) 2820–2826, https://doi.org/10.1007/BF00356225.
[11] Y. Zhang, Z. Wei, L. Shi, M. Xi, Characterization of laser powder deposited Ti-TiC composites and functional gradient materials, J. Mater. Process. Technol. 206 (2008) 438–444, https://doi.org/10.1016/j.jmatprotec.2007.12.055.
[12] R.M. Mahamood, E.T. Akinlabi, Laser metal deposition of functionally graded Ti6Al4V/TiC, Mater. Des. 84 (2015) 402–410, https://doi.org/10.1016/j.matdes.2015.06.135.
[13] L. Li, J. Wang, P. Lin, H. Liu, Microstructure and mechanical properties of functionally graded TiCp/Ti6Al4V composite fabricated by laser melting deposition, Ceram. Int. 43 (2017) 16638–16651, https://doi.org/10.1016/j.ceramint.2017.09.054.
[14] J.M. Wilson, Y.C. Shin, Microstructure and wear properties of laser-deposited functionally graded Inconel 690 reinforced with TiC, Surf. Coating. Technol. 207 (2012) 517–522, https://doi.org/10.1016/j.surfcoat.2012.07.058.
[15] Y. Shi, Y. Li, J. Liu, Z. Yuan, Investigation on the parameter optimization and performance of laser cladding a gradient composite coating by a mixed powder of Co50 and Ni/WC on 20CrMnTi low carbon alloy steel, Opt Laser. Technol. 99 (2018) 256–270, https://doi.org/10.1016/j.optlastec.2017.09.010.
[16] Q. Wang, Q. Li, L. Zhang, D. Xu, H. Jin, J. Dong, J. Wei, C. Yan, Microstructure and properties of Ni-WC gradient composite coating prepared by laser cladding, Ceram. Int. 48 (2022) 7905–7917, https://doi.org/10.1016/j.ceramint.2021.11.338.
[17] X.C. Li, J. Stampfl, F.B. Prinz, Mechanical and thermal expansion behavior of laser deposited metal matrix composites of Invar and TiC, Mater. Sci. Eng.A 282 (2000) 86–90, https://doi.org/10.1016/s0921-5093(99)00781-9.
[18] M. Ostolaza, J.I. Arrizubieta, M. Cortina, A. Lamikiz, Study of the reinforcement phase dilution into the metal matrix in functionally graded Stellite 6 and WC metal matrix composite by Laser Metal Deposition, Procedia CIRP 94 (2020) 330–335, https://doi.org/10.1016/j.procir.2020.09.062.
[19] K. Zhao, G. Zhang, G. Ma, C. Shen, D. Wu, Microstructure and mechanical properties of titanium alloy/zirconia functionally graded materials prepared by laser additive manufacturing, J. Manuf. Process. 56 (2020) 616–622, https://doi.org/10.1016/j.jmapro.2020.05.044.
[20] J.P. Kelly, J.W. Elmer, F.J. Ryerson, J.R.I. Lee, J.J. Haslam, Directed energy deposition additive manufacturing of functionally graded Al-W composites, Addit. Manuf. 39 (2021), 101845, https://doi.org/10.1016/j.addma.2021.101845.
[21] S. Saroj, C.K. Sahoo, M. Masanta, Microstructure and mechanical performance of TiC-Inconel825 composite coating deposited on AISI 304 steel by TIG cladding process, J. Mater. Process. Technol. 249 (2017) 490–501, https://doi.org/10.1016/j.jmatprotec.2017.06.042.
[22] D. Tijo, M. Masanta, A.K. Das, In-situ TiC-TiB_2 coating on Ti-6Al-4V alloy by tungsten inert gas (TIG) cladding method: Part-I. Microstructure evolution, Surf. Coating. Technol. 344 (2018) 541–552, https://doi.org/10.1016/j.surfcoat.2018.03.082.
[23] M. Wang, H. Cui, N. Wei, L. Ding, X. Zhang, Y. Zhao, C. Wang, Q. Song, A new design of in situ Ti(C, N) reinforced composite coatings and their microstructures, interfaces, and wear resistances, ACS Appl. Mater. Interfaces 10 (2018) 4250–4265, https://doi.org/10.1021/acsami.7b17286.
[24] N. Li, W. Liu, H. Xiong, R. Qin, S. Huang, G. Zhang, C. Gao, In-situ reaction of Ti-Si-C composite powder and formation mechanism of laser deposited Ti6Al4V/(TiC+Ti_3SiC_2) system functionally graded material, Mater. Des. 183 (2019), 108155, https://doi.org/10.1016/j.matdes.2019.108155.
[25] J. Liang, X. Yin, Z. Lin, S. Chen, C. Liu, C. Wang, Microstructure and wear behaviors of laser cladding in-situ synthetic (TiBx+TiC)/(Ti_2Ni+TiNi) gradient composite coatings, Vacuum 176 (2020), 109305, https://doi.org/10.1016/j.vacuum.2020.109305.
[26] Y. Zhao, L. Chen, J. Sun, W. Wu, T. Yu, Microstructure evolution and wear resistance of in-situ synthesized (Ti, Nb)C ceramic reinforced Ni204 composite coatings, Ceram. Int. (2022), https://doi.org/10.1016/j.ceramint.2022.03.016.
[27] G. Yan, M. Zheng, Z. Ye, J. Gu, C. Li, C. Wu, B. Wang, In-situ Ti(C, N) reinforced AlCoCrFeNiSi-based high entropy alloy coating with functional gradient double-layer structure fabricated by laser cladding, J. Alloys Compd. 886 (2021), 161252, https://doi.org/10.1016/j.jallcom.2021.161252.
[28] Y. Li, D. Zhang, W. Cong, Feasibility study of adding buffer layers for the laser deposition of high-ceramic content (TiB + TiC) – Ti coatings using B_4C/Ti powders, Ceram. Int. (2022), https://doi.org/10.1016/j.ceramint.2022.04.330.
[29] K.D. Traxel, A. Bandyopadhyay, Influence of in situ ceramic reinforcement towards tailoring titanium matrix composites using laser-based additive manufacturing, Addit. Manuf. 31 (2020), 101004, https://doi.org/10.1016/j.addma.2019.101004.
[30] L. Chen, T. Yu, P. Xu, B. Zhang, In-situ NbC reinforced Fe-based coating by laser cladding: simulation and experiment, Surf. Coating. Technol. 412 (2021), 127027, https://doi.org/10.1016/j.surfcoat.2021.127027.
[31] Y. Zhao, T. Zhang, L. Chen, T. Yu, J. Sun, C. Guan, Microstructure and mechanical properties of Ti–C–TiN-reinforced Ni204-based laser-cladding composite coating, Ceram. Int. 47 (2021) 5918–5928, https://doi.org/10.1016/j.ceramint.2020.11.054.
[32] L. Chen, T. Yu, X. Chen, Y. Zhao, C. Guan, Process optimization, microstructure and microhardness of coaxial laser cladding TiC reinforced Ni-based composite coatings, Opt Laser. Technol. 152 (2022), 108129, https://doi.org/10.1016/j.optlastec.2022.108129.
[33] D. Tijo, M. Masanta, In-situ TiC-TiB2 coating on Ti-6Al-4V alloy by tungsten inert gas (TIG) cladding method: Part-II. Mechanical performance, Surf. Coating. Technol. 344 (2018) 579–589, https://doi.org/10.1016/j.surfcoat.2018.03.083.
[34] R. Saeedi, R. Shoja Razavi, S.R. Bakhshi, M. Erfanmanesh, A. Ahmadi Bani, Optimization and characterization of laser cladding of NiCr and NiCr–TiC composite coatings on AISI 420 stainless steel, Ceram. Int. 47 (2021) 4097–4110, https://doi.org/10.1016/j.ceramint.2020.09.284.
[35] Y. Zhao, L. Chen, J. Sun, T. Yu, Mechanical property of YCF101 coating under different overlap modes by laser cladding, Optik 212 (2020), 164714, https://doi.org/10.1016/j.ijleo.2020.164714.
[36] L. Chen, Y. Zhao, X. Chen, T. Yu, P. Xu, Repair of spline shaft by laser-cladding coarse TiC reinforced Ni-based coating: process, microstructure and properties, Ceram. Int. 47 (2021) 30113–30128, https://doi.org/10.1016/j.ceramint.2021.07.189.
[37] H. Zeinali Moghaddam, M. Sharifitabar, G. Roudini, Microstructure and wear properties of Fe–TiC composite coatings produced by submerged arc cladding process using ferroalloy powder mixtures, Surf. Coating. Technol. 361 (2019) 91–101, https://doi.org/10.1016/j.surfcoat.2019.01.053.
[38] B. Song, T. Yu, X. Jiang, W. Xi, X. Lin, Z. Ma, Z. Wang, Development of the molten pool and solidification characterization in single bead multilayer direct energy deposition, Addit. Manuf. 49 (2022), 102479, https://doi.org/10.1016/j.addma.2021.102479.
[39] L. Chen, T. Yu, C. Guan, Y. Zhao, Microstructure and properties of metal parts remanufactured by laser cladding TiC and TiB_2 reinforced Fe-based coatings, Ceram. Int. 48 (2022) 14127–14140, https://doi.org/10.1016/j.ceramint.2022.01.299.
[40] D. Vallauri, I.C. Atías Adrián, A. Chrysanthou, TiC-TiB_2 composites: a review of phase relationships, processing and properties, J. Eur. Ceram. Soc. 28 (2008) 1697–1713, https://doi.org/10.1016/j.jeurceramsoc.2007.11.011.
[41] Y. Liu, L. Yang, X. Yang, T. Zhang, R. Sun, Optimization of microstructure and properties of composite coatings by laser cladding on titanium alloy, Ceram. Int. 47 (2021) 2230–2243, https://doi.org/10.1016/j.ceramint.2020.09.063.
[42] Q. Wu, W. Li, N. Zhong, W. Gang, W. Haishan, Microstructure and wear behavior of laser cladding VC-Cr_7C_3 ceramic coating on steel substrate, Mater. Des. 49 (2013) 10–18, https://doi.org/10.1016/j.matdes.2013.01.067.
[43] L. Chen, Y. Zhao, F. Meng, T. Yu, Z. Ma, S. Qu, Effect of TiC content on the microstructure and wear performance of in situ synthesized Ni-based composite coatings by laser direct energy deposition, Surf. Coat. Technol. 444 (2022), 128678, https://doi.org/10.1016/j.surfcoat.2022.128678.
[44] Y. Zhao, T. Yu, L. Chen, Y. Chen, C. Guan, J. Sun, Microstructure and wear resistance behavior of Ti–C–B_4C-reinforced composite coating, Ceram. Int. 46 (2020) 25136–25148, https://doi.org/10.1016/j.ceramint.2020.06.300.
[45] M. Ansari, E. Jabari, E. Toyserkani, Opportunities and challenges in additive manufacturing of functionally graded metallic materials via powder-fed laser directed energy deposition: a review, J. Mater. Process. Technol. 294 (2021), 117117, https://doi.org/10.1016/j.jmatprotec.2021.117117.
[46] Z. Tong, H. Liu, J. Jiao, W. Zhou, Y. Yang, X. Ren, Laser additive manufacturing of CrMnFeCoNi high entropy alloy : microstructural evolution, high-temperature oxidation behavior and mechanism, Opt Laser. Technol. 130 (2020), 106326, https://doi.org/10.1016/j.optlastec.2020.106326.
[47] M.J. Bermingham, D.H. StJohn, J. Krynen, S. Tedman-Jones, M.S. Dargusch, Promoting the columnar to equiaxed transition and grain refinement of titanium alloys during additive manufacturing, Acta Mater. 168 (2019) 261–274, https://doi.org/10.1016/j.actamat.2019.02.020.
[48] L. Chen, Y. Zhao, B. Song, T. Yu, Z. Liu, Modeling and simulation of 3D geometry prediction and dynamic solidification behavior of Fe-based coatings by laser cladding, Opt Laser. Technol. 139 (2021), 107009, https://doi.org/10.1016/j.optlastec.2021.107009.
[49] B. Song, T. Yu, X. Jiang, W. Xi, X. Lin, The relationship between convection mechanism and solidification structure of the iron-based molten pool in metal laser direct deposition, Int. J. Mech. Sci. 165 (2020), https://doi.org/10.1016/j.ijmecsci.2019.105207.
[50] B.E. Carroll, R.A. Otis, J.P. Borgonia, J.O. Suh, R.P. Dillon, A.A. Shapiro, D. C. Hofmann, Z.K. Liu, A.M. Beese, Functionally graded material of 304L stainless steel and inconel 625 fabricated by directed energy deposition: characterization and thermodynamic modeling, Acta Mater. 108 (2016) 46–54, https://doi.org/10.1016/j.actamat.2016.02.019.
[51] W. Meng, W. Zhang, W. Zhang, X. Yin, B. Cui, Fabrication of steel-Inconel functionally graded materials by laser melting deposition integrating with laser synchronous preheating, Opt Laser. Technol. 131 (2020), 106451, https://doi.org/10.1016/j.optlastec.2020.106451.
[52] M. Qunshuang, L. Yajiang, W. Juan, Effects of Ti addition on microstructure homogenization and wear resistance of wide-band laser clad Ni60/WC composite coatings, Int. J. Refract. Met. Hard Mater. 64 (2017) 225–233, https://doi.org/10.1016/j.ijrmhm.2016.11.002.
[53] W. Zhou, N. Takase, M. Dong, N. Watanabe, S. Guo, Z. Zhou, N. Nomura, Elucidating the impact of severe oxidation on the powder properties and laser melting behaviors, materials & design, J 221 (2022), https://doi.org/10.1016/j.matdes.2022.110959, 110959.
[54] Y. Lin, C. Jiang, Z. Lin, Q. Chen, Y. Lei, H. Fu, Laser in-situ synthesis of high aspect ratio TiB fiber bundle reinforced titanium matrix composite coating, Opt Laser. Technol. 115 (2019) 364–373, https://doi.org/10.1016/j.optlastec.2019.02.047.
[55] G. Muvvala, S. Mullick, A.K. Nath, Development of process maps based on molten pool thermal history during laser cladding of Inconel 718/TiC metal matrix composite coatings, Surf. Coating. Technol. 399 (2020), https://doi.org/10.1016/j.surfcoat.2020.126100.
[56] M. Xie, C. Wu, S. Zhou, J. Jin, S. Zhao, D. Chen, TiB_2- and Fe_2P with nanotwins-reinforced Cu-based immiscible composites fabricated by selective laser melting:

formation mechanism and wear behavior, J. Alloys Compd. 864 (2021), 158716, https://doi.org/10.1016/j.jallcom.2021.158716.
[57] A. Emamian, S.F. Corbin, A. Khajepour, Tribology characteristics of in-situ laser deposition of Fe-TiC, Surf. Coating. Technol. 206 (2012) 4495–4501, https://doi.org/10.1016/j.surfcoat.2012.01.051.
[58] Z. Ma, Q. Wang, H. Chen, L. Chen, S. Qu, Z. Wang, T. Yu, A grinding force predictive model and experimental validation for the laser-assisted grinding (LAG) process of zirconia ceramic, J. Mater. Process. Technol. 302 (2022), https://doi.org/10.1016/j.jmatprotec.2022.117492.
[59] Z. Tong, H. Liu, J. Jiao, W. Zhou, Y. Yang, X. Ren, Microstructure, microhardness and residual stress of laser additive manufactured CoCrFeMnNi high-entropy alloy subjected to laser shock peening, J. Mater. Process. Technol. 285 (2020), 116806, https://doi.org/10.1016/j.jmatprotec.2020.116806.
[60] L. Chen, Y. Zhao, C. Guan, T. Yu, Effects of CeO_2 addition on microstructure and properties of ceramics reinforced Fe-based coatings by laser cladding, Int. J. Adv. Manuf. Technol. 115 (2021) 2581–2593, https://doi.org/10.1007/s00170-021-07297-8.
[61] Y. Sun, L. Jin, Y. Gong, X. Wen, G. Yin, Q. Wen, B. Tang, Experimental evaluation of surface generation and force time-varying characteristics of curvilinear grooved micro end mills fabricated by EDM, J. Manuf. Processes 73 (2022) 799–814, https://doi.org/10.1016/j.jmapro.2021.11.049.
[62] Y. Zhao, T. Yu, J. Sun, S. Jiang, Microstructure and properties of laser cladded B_4C/TiC/Ni-based composite coating, Int. J. Refract. Met. Hard Mater. 86 (2020), 105112, https://doi.org/10.1016/j.ijrmhm.2019.105112.
[63] Y. Guo, C. Li, M. Zeng, J. Wang, P. Deng, Y. Wang, In-situ TiC reinforced $CoCrCuFeNiSi_{0.2}$ high-entropy alloy coatings designed for enhanced wear performance by laser cladding, Mater. Chem. Phys. 242 (2020), 122522, https://doi.org/10.1016/j.matchemphys.2019.122522.
[64] S. Zhou, M. Xie, C. Wu, Y. Yi, D. Chen, L.C. Zhang, Selective laser melting of bulk immiscible alloy with enhanced strength: heterogeneous microstructure and deformation mechanisms, J. Mater. Sci. Technol. 104 (2022) 81–87, https://doi.org/10.1016/j.jmst.2021.06.062.
[65] R.J. Moat, A.J. Pinkerton, L. Li, P.J. Withers, M. Preuss, Residual stresses in laser direct metal deposited Waspaloy, Mater. Sci. Eng.A 528 (2011) 2288–2298, https://doi.org/10.1016/j.msea.2010.12.010.
[66] G. Qiao, B. Zhang, Q. Bai, Y. Gao, W. Du, Y. Zhang, Machinability of TiC-reinforced titanium matrix composites fabricated by additive manufacturing, J. Manuf. Process. 76 (2022) 412–418, https://doi.org/10.1016/j.jmapro.2022.02.033.